 doi:10.20944/preprints202207.0104.v1

Article

Numerical Investigation of Photo Generated Carrier Recombination Dynamics on the Device Characteristics for the Perovskite/Carbon Nitride Absorber Layer Solar Cell

Faisal Saeed[1, 2*], Muhammad Haseeb Khan[2], Haider Ali Tauqeer[2], Asfand Haroon[3], Asad Idrees[2], Syed Mzhar Shehrazi[4]

[1] Department of Physics, Functional Materials and Optoelectronic Devices (FMOD) Lab, Lahore University of Management Sciences (LUMS), Lahore, 54792, Punjab, Pakistan
[2] Department of Electrical Engineering, Lahore University of Management Sciences (LUMS), Punjab, 54792, Pakistan
[3] Department of Electrical Engineering, University of Engineering and Technology Lahore, Punjab, 39161, Pakistan
[4] Department of Electrical Engineering, University of Lahore, Lahore, Punjab, 54590, Pakistan

* Correspondence: Faisal Saeed-19060005@lums.edu.pk

Abstract: Herein we foremost detailed the numerical modeling of the double absorber layer- methyl ammonium lead iodide ($CH_3NH_3PbI_3$) – carbon nitride (C_2N) layer solar cell and subsequently provided in-depth insight on the active layer associated with dominant radiative and non-radiative recombination losses limiting the efficiency (η) of the solar cell. Under recombination kinetics phenomena, we explored the influence of Radiative recombination, Auger recombination, Shockley Read Hall recombination, the energy distribution of defects; Band Tail recombination (Hoping Model), Gaussian distribution, metastable defect states including single donor (0/+), single acceptor (-/0), Double Donor (0/+/2+), double acceptor (2/-/0-), and the interface layer defects on the output characteristics of the solar cell. Setting defect (or trap) density to $10^{15}cm^{-3}$ with uniform energy distribution of defects for all the layers, we achieved the η of 24. 16 %. A considerable enhancement in power conversion efficiency (η~27 %) was perceived as we reduced the trap density to $10^{14}cm^{-3}$ for the absorber layers. Further, it was observed that for the absorber layer with double donor defect states, the active layer should be carefully synthesized to reduce crystal order defects to keep the total defect density as low as $10^{17}cm^{-3}$ to achieve efficient device characteristics.

Keywords: Double Absorber Layer Solar Cell; Recombination; Numerical Investigation

1. Introduction

Presently photovoltaic modules based on wafer-based crystalline silicon solar cells account for > 90% of the global photovoltaic market[1–5]. Laudable enhancement in power conversion efficiency (η) has been experienced for this technology over the last few years leading to the thin film, tandem, and various lab-based architectures[6–13]. On top of that, the manufacturing process of crystalline-based solar modules requires expensive materials and production costs. Given that, double absorber layer (DAL) solar cells rivaling the tandem solar cells can be considered a promising candidate among emerging photovoltaic technology for achieving high device performance in cut down cost [14].

Despite the perceptible advancement in tandem solar cells (perovskite/silicon tandem solar reported recently with impressive η ~29.15% [15]), ease of fabricating DAL solar cells is one of the major advantages against the complexity in tuning 2 terminal tandem solar cells or managing the 4 terminal tandem device circuitry. Besides this, DAL solar

Preprints (www.preprints.org) | NOT PEER-REVIEWED | Posted: 7 July 2022 doi:10.20944/preprints202207.0104.v1

cells can be characterized by low production cost compared to tandem solar cells making them a potential candidate for the future photovoltaic industry [16].

The composition of DAL solar cells requires the absorber layers (or active layers) to have an almost similar lattice structure[16]. The active layers can be chalcogenides, perovskites, polymers, or other organic/inorganic layers. In such architecture, the absorber layer with varied energy band gap forming the junction sequentially harness photo-generated power from their respective portions of the solar spectrum. This makes the multi-junction devices efficient and comparable to the single junction ones. However, the success of such DAL devices lies in the current matching of the active layer junctions and efficient recombination of photo-generated carriers from the adjacent junctions.

So far limited literature is reported on the theoretical modeling/fabrication of DAL solar cells. Ho Yeon, Deuk, *et al.* [17] reported a 4 % efficient PbS/Cds solar cell fabricated by chemical bath deposition. Ahmad, Faiz *et al* [14] theoretically proposed optical modeling of $CuIn_{1-\xi_1}Ga_{\xi_1}Se_2$ / $Cu_2ZnSn(S_{\xi_2}Se_{1-\xi_2})$ absorber layer solar cell with an impressive $\eta \sim 34.45\%$. AlZoubi, Tariq, *et al* [18] detailed numerical modeling of CZTS/Si-based active layer solar cell having $\eta \sim 29.15\%$. Maurya, K *et al*.[19] computationally detailed > 35% efficient thin-film device based on Sb_2Se_3/CZTS absorber layer. S Yasin *et al* [16] recently detailed $C_2N/FASnI_3$ absorber layer solar cell with $\eta \sim 25.15\%$ keeping the trap density $10^{14}cm^{-3}$.

Here we proposed a novel structured DAL employing metal halide perovskite and Carbon Nitride (C_2N) as the absorber layers. Carbon Nitride (C_2N) is a 2D material with a structural composition similar to graphene, wider energy band gap ~ 1.8 eV, and a higher optical absorption in the visible spectrum [20–23]. C_2N material has favorable properties to be used as a primary absorber for photovoltaic applications. It has been explored numerically for photovoltaic cell modeling but is not reported in the practical study yet. We, therefore, focused on a defect-based study for the absorber layers to comprehensively investigate the proposed active layered structure solar cell favorability for future thin-film photovoltaic applications.

2. Numerical Modeling and Material Parameters

The proposed solar cell is the architecture of FTO/TiO_2/C_2N/ $CH_3NH_3PbI_3$/ Au-back metal contact (see Fig. 1) and was numerically modeled and investigated in SCAPS-1D which is based on three coupled semiconductor differential equations; Poisson's equation, and the continuity equations for electrons and holes (1) [24–26] . The material parameters for the simulation are enlisted in Appendix A Table A. The SCAPS numerically evaluates the steady-state solution of these equations with appropriate boundary conditions[27]v.

$$\begin{cases} \nabla^2 V(x) = \frac{q}{\varepsilon}\left[p(x) - n(x) + {N_D}^+(x) - {N_A}^-(x) + {N_{tr}}^{\pm}\right] \\ \frac{\partial p(n)}{\partial t} = G_p - \frac{p_n - p_{no}}{\tau_p} - p_n\mu_p\frac{d\xi}{dx} + \mu_p\xi\frac{dp_n}{dx} + D_p\frac{d^2p_n}{dx^2} \\ \frac{dn_p}{dt} = G_n - \frac{n_p - n_{po}}{\tau_n} - n_p\mu_n\frac{d\xi}{dx} + \mu_n\xi\frac{dn_p}{dx} + D_p\frac{d^2n_p}{dx^2} \end{cases} \quad (1)$$

Where $\nabla^2 V$the electrostatic potential, q is the electronic charge, $p(x)$ and $n(x)$ are the position-dependent hole and electron concentration, ${N_D}^+(x)$ and ${N_A}^-(x)$ is the position-dependent ionized dopant and acceptor concentration, ${N_{tr}}^{\pm}$ is the shallow/bulk trap (or defect) carrier concentration. The electron-hole pair generation, $G(x)$in the absorber layer as a result of incident photon flux (N_{phot}) of wavelength (λ) at each position (x) within the layer follows the mathematical relation (2) [28]. λ_{min}, λ_{max} are the minimum and maximum wavelengths of the incoming solar spectrum.

Preprints (www.preprints.org) | NOT PEER-REVIEWED | Posted: 7 July 2022 doi:10.20944/preprints202207.0104.v1

$$G(\lambda,x) = \alpha\big((\lambda,x)\big).N_{phot}(\lambda,x) = \int_{\lambda_{min}}^{\lambda_{max}} G(\lambda,x)\,d\lambda$$
$$= \int_{\lambda_{min}}^{\lambda_{max}} \alpha\big((\lambda,x)\big).N_{phot}(\lambda,x)d\lambda \qquad (2)$$

Where in,

$$N_{phot}(\lambda,x) = N_{photo}(\lambda).T_{front}(\lambda).\exp\big(-x\alpha(\lambda)\big).\frac{1+R_{back}(\lambda)\exp(-2(d-x)\alpha(\lambda))}{1-R_{back}(\lambda)R_{int}\exp(-2d\alpha(\lambda))} \qquad (3)$$

In the above equation, $T_{front}(\lambda)$ is the transmission at the front contact (wavelength dependent), $R_{back}(\lambda)$ is the reflection at the back contact (wavelength dependent), R_{int} is the internal reflection at the front contact, d is the layer thickness.

Further, we employed one of the four SCAPS inbuilt optical absorption (α) models following the expression (4) [28]. In this model energy band gap (E_g) follows the square root law and $\alpha = 0$ if the incident photon energy is $< E_g$.

$$\alpha(h\nu) = \left(\alpha_o + \frac{\beta_o E_g}{h\nu}\right)\sqrt{\frac{h\nu}{E_g} - 1} \qquad (4)$$

The adoption of C_2N absorber layer with perovskite active layer aided in better utilization of solar spectrum as can be observed in Figure 2 (a). The device with optimized thicknesses demonstrated η of 24.17%, open-circuit voltage (V_{oc}) of 1.22 V, short circuit current density (J_{sc}) of 23.6392 mA/cm^2 and the fill factor (FF) of 83.27% while the current density-voltage curve of the DAL solar under standard illumination conditions is depicted in Figure 2 (b). Figure 3 (c) illustrates the energy level diagram of the solar cell. Further, the external quantum efficiency of the solar cell (see Figure 2(d)) remained > 90% for the near-ultraviolet region (360 $nm \leq$ incident light $\geq$ 360 nm or photon energy, E_p~3.44 eV) to the major part of the visible light spectrum (incident light wavelengths $\leq$ 360 nm or E_p~ 3.44 eV).

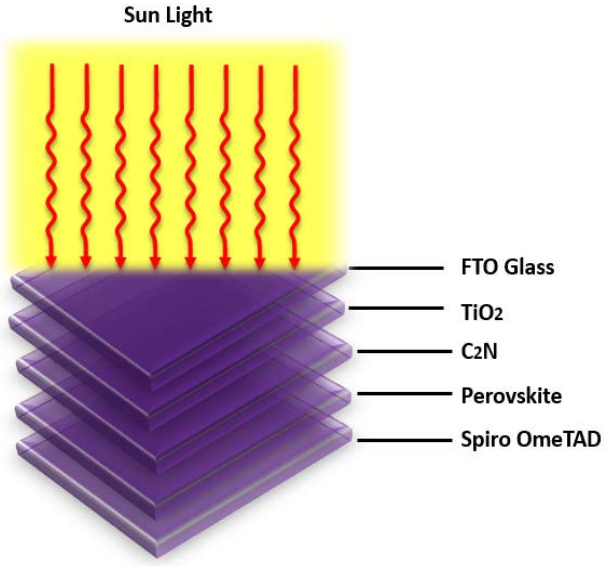

Figure 1. Proposed double Absorber Layer solar cell layer structure

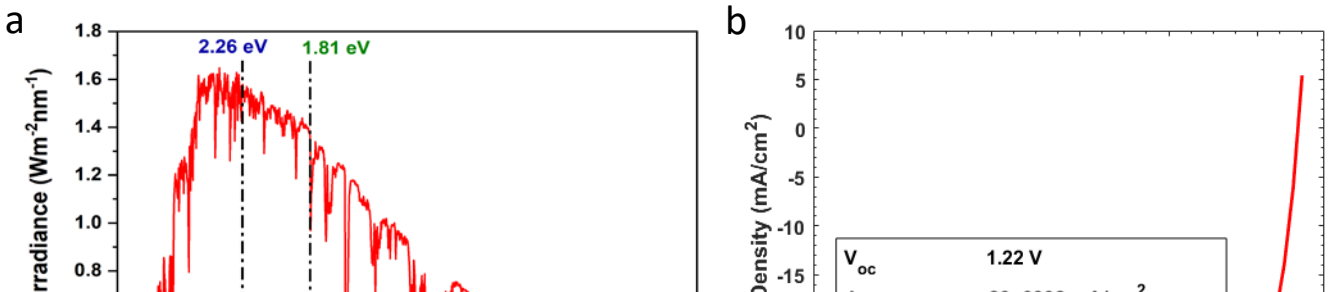

Preprints (www.preprints.org) | NOT PEER-REVIEWED | Posted: 7 July 2022 doi:10.20944/preprints202207.0104.v1

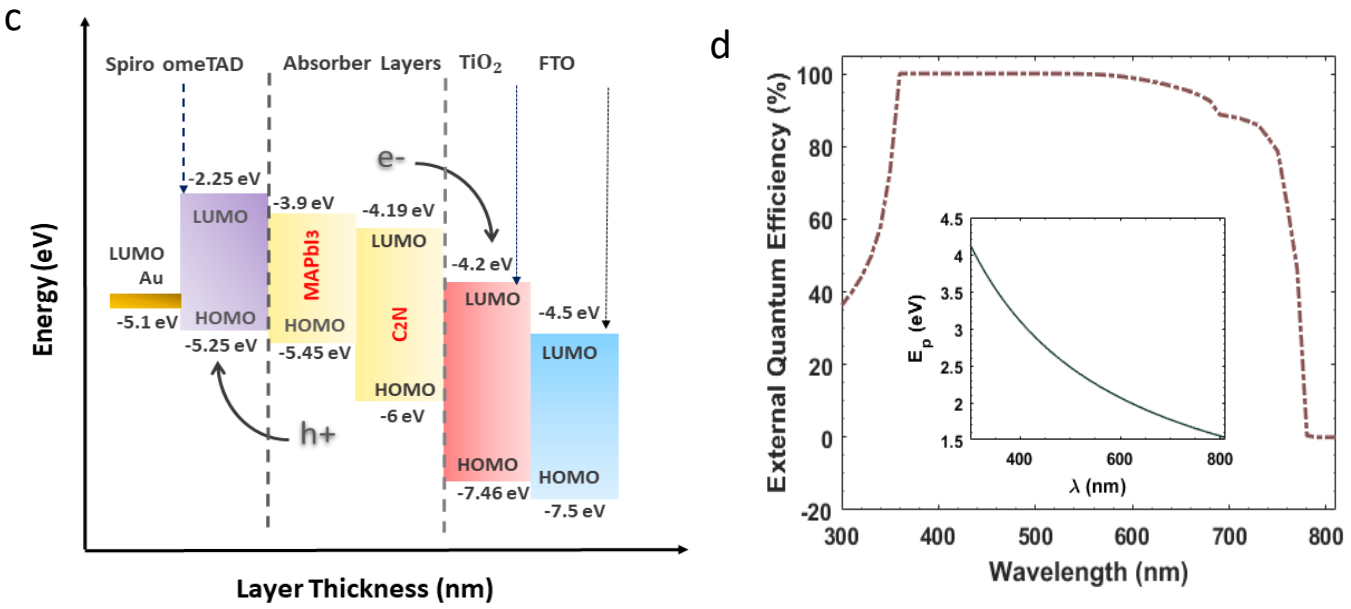

Figure 2. The (a) AM 1.5 G Solar spectrum utilization approach using double absorber layer in solar cell (b) current density-voltage characteristics of the solar (c) energy level diagram of the double absorber layer solar cell (d) external quantum efficiency of the solar cell. Figure shown inside (d) is illustrating the variartion in photonenergy,E_p with respect to incident light wavelength

3. Results and Discussions

3.1. Influence of Recombination on Device Performance

Ideally photovoltaic material has a higher absorption coefficient to effectively harvest incident solar energy photons and convert them into free charge carriers. However, recombination losses in solar cells are inevitable due to material defects [29]. Recombination losses affect the collection current as well as forward bias injection current. This directly influences the short circuit current density and open-circuit voltage of the solar cell thereby limiting the fill factor and efficiency of the solar cell [30]. Recombination mechanisms considered in this investigation for the $CH_3NH_3PbI_3/C_2N$ absorber layer include Radiative recombination (R_{Rad}), Auger (R_{Aug}) and Shockley Read Hall recombination (R_{SRH}) following the expression (5). More insight into the recombination phenomenon is provided in Figure 3.

Preprints (www.preprints.org) | NOT PEER-REVIEWED | Posted: 7 July 2022 doi:10.20944/preprints202207.0104.v1

$$\begin{cases} R = R_{Rad} + R_{Aug} + R_{SRH} \\ R_{Rad} = K\,(np - n_i^2) \\ R_{Aug} = \left(C_{n,aug}n + C_{n,aug}p\right)(np - n_i^2) \\ R_{SRH} = \frac{(np - n_i^2)}{\tau_p\left(n + ni\exp\left(\frac{E_t - E_i}{kT}\right)\right) + \tau_n\left(p + ni\exp\left(\frac{E_i - E_t}{kT}\right)\right)} \end{cases} \quad (5)$$

Where K is the radiative recombination coefficient, C_n^A (C_p^A) is the Auger electron (hole) recombination coefficient, n (p) is the electron (hole) carrier concentration, τ_n (τ_p) is the electron (hole) carrier lifetime, E_i is the intrinsic energy level, E_t is the trap energy level, T is the temperature at room temperature. The K factor for $CH_3NH_3PbI_3$ as calculated by first-principles is reported in the range of (0.5-1.5)$\times 10^{-9}$ (cm^3/s). The range of C_n^A ($C_p^A The$) factor for $CH_3NH_3PbI_3$ perovskite material as evaluated from Time and Excitation Energy-dependent photoluminescence spectroscopy has been reported to lie in between (1.8-3.7). The point defect study on C_2N confirmed that such material exhibit both direct and indirect energy bandgap nature. We, therefore, set alike the K and C_n^A ($C_p^A The$) factor for both the absorber layers. The device current density voltage characteristics under radiative, Auger, and SRH recombination are shown in Figures 4(a) , 5(a) and 6(a) respectively.

To investigate the impact of radiative recombination, we varied the K factor in the range of $10^{-8} - 10^{-14}$ (cm^3/s) (see Figure 4 (b)). An increased value of K has an adverse effect on the output characteristics of the solar cell. It was observed that the device demonstrated a maximum η ~24.17 %, $V_{oc} \sim 1.22\,V$, and J_{sc} ~23.64 mA/cm^2 at K =10^{-14} cm^3/s as illustrated in Figure 4. The highest FF ~87.31 % was obtained at K =10^{-10} cm^3/s. The device η fall down to ~16 % as we increased the K to 10^{-8} cm^3/s. To investigate the influence of R_{Aug} on the device performance, we varied the $C_{n,aug}(C_{p,aug})$ from$10^{-25} - 10^{-31}$ (cm^6/s) (see Figure 5 (b)). The device demonstrated the maximum η at $C_{n,aug}$ =10^{-31} cm^6/s while the minimum at $C_{n,aug}$ =10^{-25} cm^6/s. To analyze R_{SRH}, we employed the trap density model as it has been elaborated in previous studies. The trap density for the double absorber layer, $N_{tr,DAL}$ was varied in the range of $10^{14} - 10^{17}$ cm^{-3} (see Figure 6 (b)). As discussed earlier, the device has been simulated with a defect density of 10^{15} cm^{-3}. On decreasing the defect density to 10^{14} cm^{-3}, the device demonstrated maximumη ~26.18 %, $V_{oc} \sim 1.34\,V$, and J_{sc} ~26.79 mA/cm^2 and the device η is reduced to ~17 % including other device parameters as we increased the defect density to 10^{17} cm^{-3}.

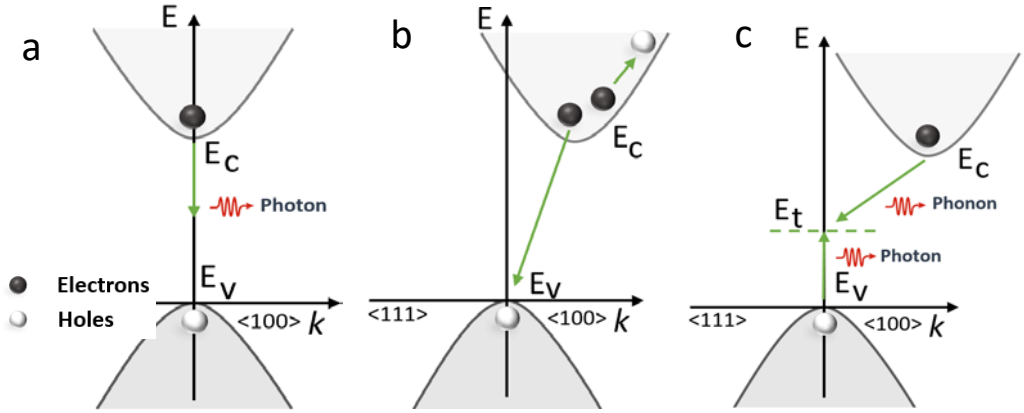

Figure 3. Photogenerated carrier recombination mechanism. (a) Radiative recombination (b) Auger recombination and (c) SRH recombination using energy (E) , momentum (K) diagram.

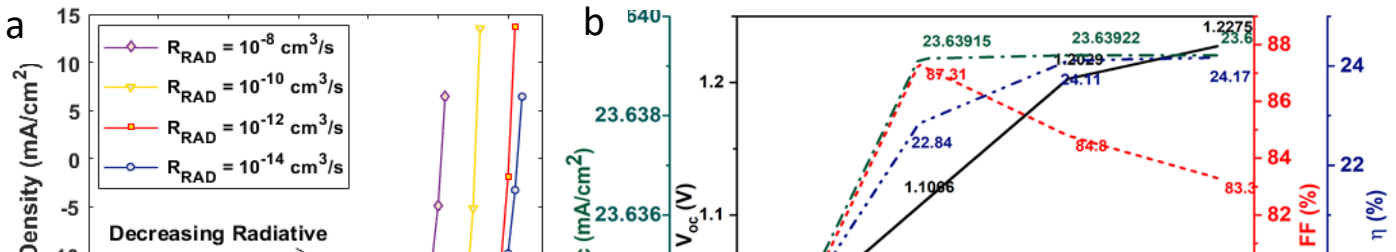

Preprints (www.preprints.org) | NOT PEER-REVIEWED | Posted: 7 July 2022 doi:10.20944/preprints202207.0104.v1

Figure 4. (a) Current density -voltage chracterestics of solar cell under radiative recombination (b) Influence of Radiative recombination on the open circuit volage, short circuit current density, fill factor and efficiency the solar cell.

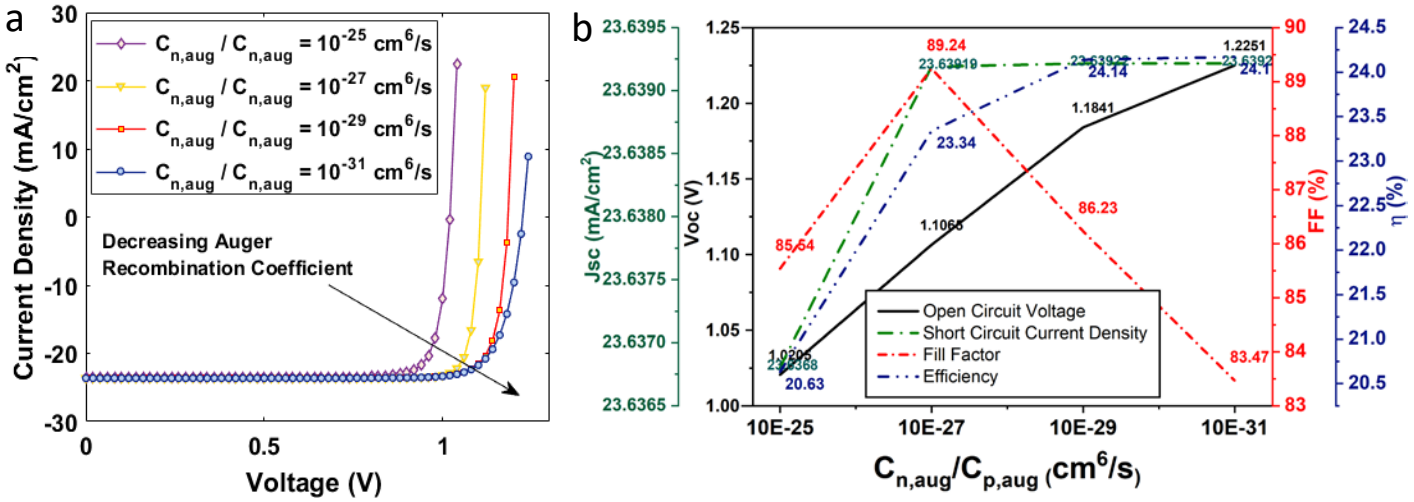

Figure 5. (a) Current density -voltage chracterestics of solar cell under auger recombination (b) Influence of Auger recombination coefficient on the open circuit volage, short circuit current density, fill factor and efficiency the solar cell.

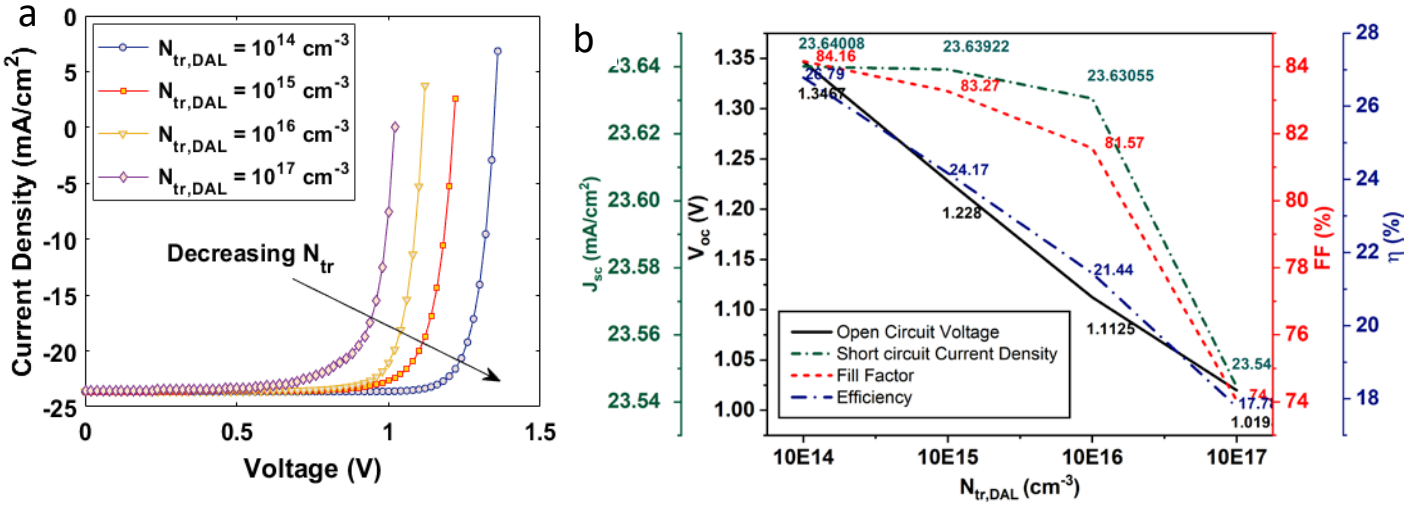

Figure 6. (a) Current density -voltage chracterestics of solar cell under auger recombination (b) Influence of defect denisty assited SRH recombination on the open circuit volage, short circuit current density, fill factor and efficiency the solar cell.

3.2 Influence of Energy Distribution of Defects on the Device Performance

Preprints (www.preprints.org) | NOT PEER-REVIEWED | Posted: 7 July 2022 doi:10.20944/preprints202207.0104.v1

In organic-inorganic absorber layers, the energy distribution of defects modeling is imperative to accurately model the device. The total defect density of state (DOS) in the absorber layer is assumed to be comprised of shallow level defects modeled by exponentially decaying conduction or valence band tail states and deep level defects modeled by Gaussian distribution in mid gaps (see Figure 7 (a))[31,32] . The Gaussian, conduction/valence band tail state and energy distribution in the SCAPS environment follow the mathematical relation (6-8) [28]wherein E_t is the trap energy level, E_c is the characteristic energy, w_G is the width of Gaussian energy distribution, w_t is the width of tail-like distribution, $N_t(E)$ is the defect density in cm^{-3}/eV, N_{peak} is the peak density of the energy distribution. Band tailing hampers the mobility of photo-generated carriers to great extent by trapping and de-trapping. w_G $(or\ w_t)$ is related to the degree of disorder in crystal [33]. Experimentally reported values for perovskite material are in the range of $15-63\ (meV)$ [34].

We however kept the w_G as 0.564 eV while w_t= 0.1 eV for the absorber layers. The N_{peak} in all above-mentioned energy, distributions are 10^{15} $(1/eV/cm^3)$ with total defect density of states as $10^{15}\ cm^{-3}$.

$$\overbrace{Range = \left[E_t - w_G\frac{E_c}{2}; E_t + w_G\frac{E_c}{2}\right], N_t(E) = N_{peak} \times \exp\left[-\left(\frac{E-E_t}{E_c}\right)^2\right]}^{Gaussian\ Energy\ Distribution} \quad (6)$$

$$\overbrace{Range = [E_t - w_t E_c; E_t], N_t(E) = N_{peak} \times \exp\left[\frac{E-E_t}{E_c}\right]}^{Conduction\ Band\ Energy\ Distribution} \quad (7)$$

$$\overbrace{Range = [E_t; E_t + w_t E_c], N_t(E) = N_{peak} \times \exp -\left[\frac{E-E_t}{E_c}\right]}^{Valence\ Band\ Energy\ Distribution} \quad (8)$$

The device has been simulated with the above modeling and current density vs voltage characteristics are shown in Figure 7 (b). the device η was decreased to 22.12 % from 24.17 %, V_{oc} to ~1.14 V, J_{sc} to ~23.634 mA/cm^2 and FF ~81 as can be observed from Figure. The current density curve under both conditions is summarized in Table 1.

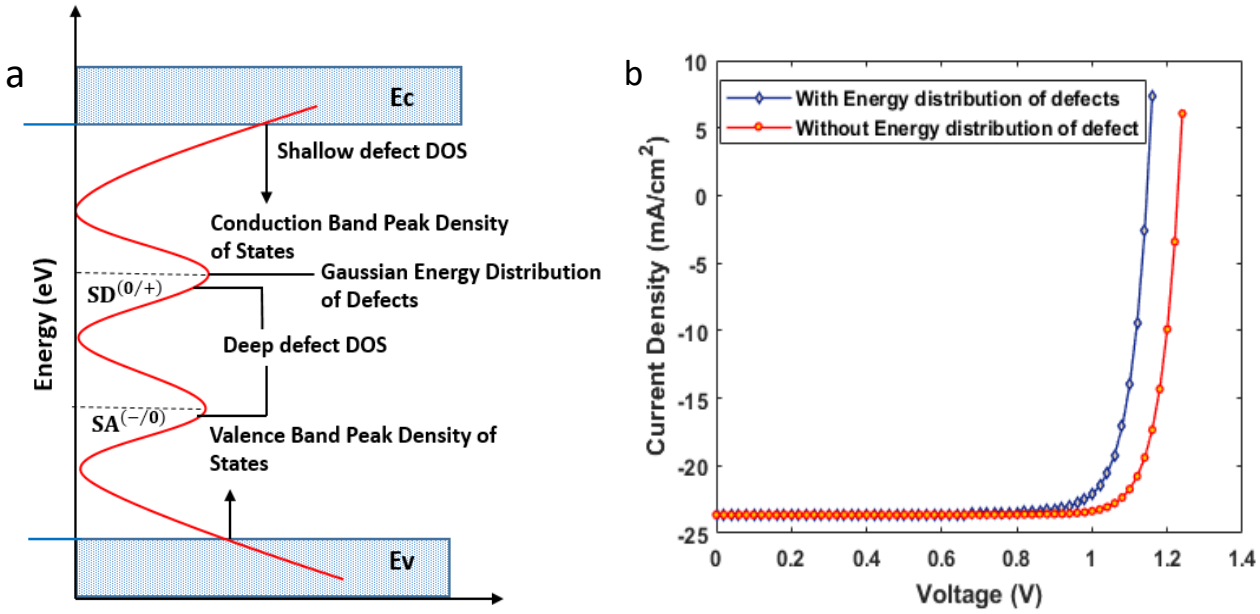

Figure 7. (a)Density of State (DOS) of semiconductor material (b) Current density-voltage characteristics for the solar cell without and adoption of energy distribution of defects

Table ects

Preprints (www.preprints.org) | NOT PEER-REVIEWED | Posted: 7 July 2022 doi:10.20944/preprints202207.0104.v1

	V_{oc} (V)	J_{sc} (mA/cm^2)	FF (%)	η (%)
Without Energy Distribution of Defects	1.22	23.692	83.92	24.17
With Energy Distribution of Defects	1.14	23.634	81.01	22.12

3.3 Influence of Metastable Defects on the Device Performance

In this section, we investigated the impact of metastable defects transition on the absorber layers. In $CH_3NH_3PbI_3$, halide ion segregation requires the migration of halide ions which is a defect-driven process resulting in halide vacancy defects [35]. For the absorber layer, we induced double vacancy defects including a single donor ($SD^{(0/+)}$), double acceptor ($SD^{(-/0)}$), double donor ($DD^{(0/+/2/+}$), double acceptor ($DA^{(2/-/0/-)}$ at varying total trap density. The single (double) donor defect states per unit volume are concentrated closer to the conduction band edge while single (double) acceptors are concentrated closer to the valence band [36,37]. The impact of metastable defects on device output characteristics at varied trap densities ($10^{14} - 10^{17}\ cm^{-3}$) is summarized in Tables 2, 3, 4, and 5 respectively. It was observed that single donor defects least affected the device output characteristics. However, $DD^{(0/+/2/+)}$ defect considerably affected solar cell performance in all conditions. The current density voltage characteristics for metastable state defects are depicted in Figure 8 a while Figure 8 (b) provides more insight into the results.

Table 2. Defect State effect on output characteristics of solar cell at trap density of $10^{17}\ cm^{-3}$

	V_{oc} (V)	J_{sc} (mA/cm^2)	FF (%)	η (%)
Single Donor	1.3467	23.64038	84.16	26.79
Single Acceptor	1.3467	23.64012	84.16	26.79
Double Donor	1.0996	23.62985	81.09	21.07
Double Acceptor	1.0997	23.62824	81.71	21.23

Table 3. Defect State effect on output characteristics of solar cell at trap density $10^{15}\ cm^{-3}$

	V_{oc} (V)	J_{sc} (mA/cm^2)	FF (%)	η (%)
Single Donor	1.228	23.63991	83.23	24.16
Single Acceptor	1.228	23.63899	83.29	24.18
Double Donor	1.005	23.29016	70.79	16.58
Double Acceptor	1.0168	23.42961	71.89	17.12

Table 4. Defect State effect on output characteristics of solar cell at trap density $10^{16}\ cm^{-3}$

	V_{oc} (V)	J_{sc} (mA/cm^2)	FF (%)	η (%)
Single Donor	1.1131	23.51052	81.76	21.4
Single Acceptor	1.115	23.45095	82.84	21.66
Double Donor	0.8839	9.829793	61.15	5.31
Double Acceptor	0.9845	16.46489	74.39	12.06

Table 5. Double donor Defect State effect on output characteristics of solar cell

Preprints (www.preprints.org) | NOT PEER-REVIEWED | Posted: 7 July 2022 doi:10.20944/preprints202207.0104.v1

	V_{oc} (V)	J_{sc} (mA/cm^2)	FF (%)	η (%)
Single Donor	1.0251	20.1563	78.86	16.29
Single Acceptor	1.0525	19.40046	82.35	16.82
Double Donor	0.7186	1.200655	63.14	0.54
Double Acceptor	1.0141	12.45877	72.17	9.12

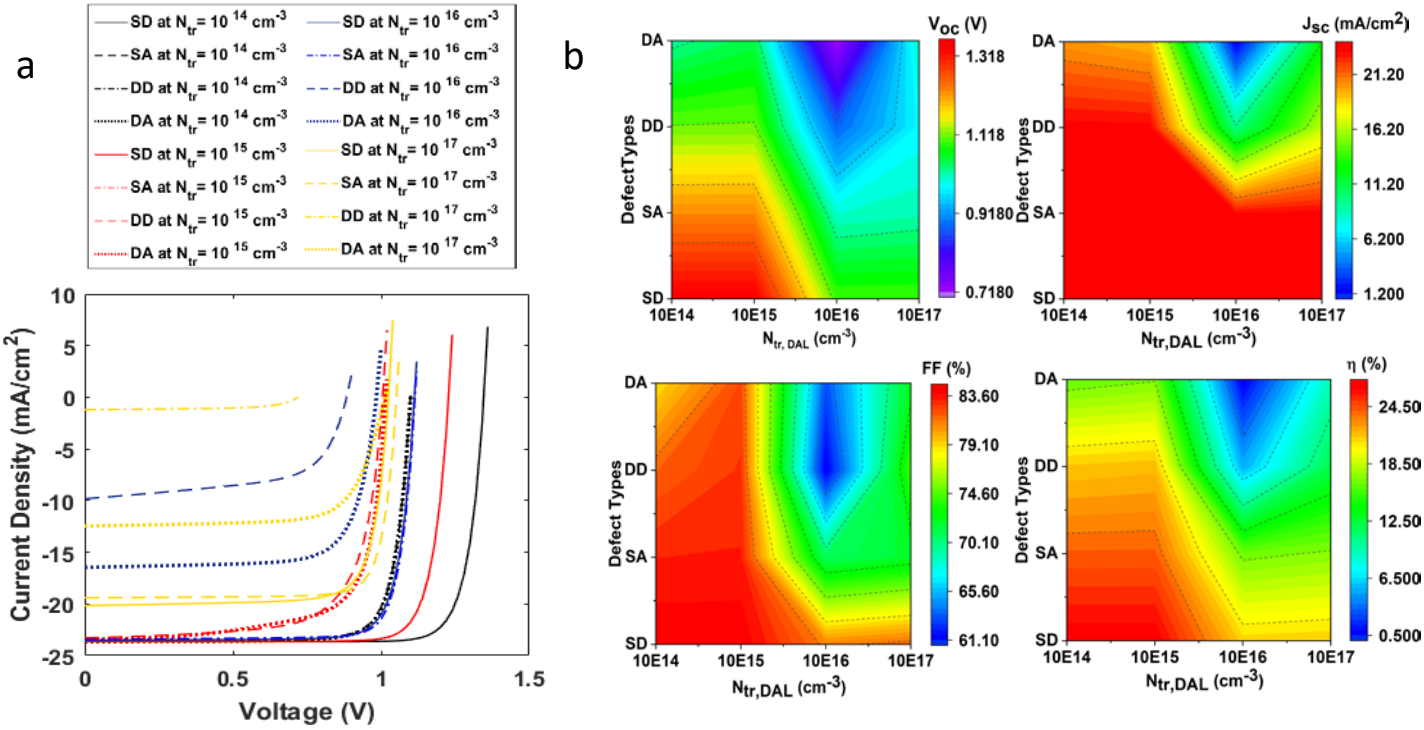

Figure 8. (a) Current-voltage characteristics solar cell on includion of metastable defect states with varying trap density (b) Influence of metstable defect states ; single donor(SD), single acceptor(SA), double donor(DD), double acceptor (DA) at varying defect density on opencircuit voltage, short circuit current denisty , fill factor and efficiency of the solar cell.

3.4 Influence of Interface Defects on the Device Performance

Interfacial recombination plays a significant role in determining the performance of the solar cell. Interface defects emerge due to recombination centers at the interface of the absorber material/hole transport layer (or electron transport layer)[38]. These recombination centers can be present inside the absorber layer or hole transport layer (or electron transport layer) at the interface. Other reasons for interface defects can be unfavorable HTL/ absorber layer (or absorber layer/ETL) band alignment and back transfer-induced recombination[39] as illustrated in Figure 9.

The current density-voltage curve shown in Figure 10(a) illustrates the effect of varying interface defect density at the hole transport layer/absorber layer interface, $N_{tr,H/A}$. The $N_{tr,H/A}$ was varied in the range of $10^{14} - 10^{17}$ (cm^{-3}). Interface defects considerably affected the device power conversion efficiency of the solar cell in comparison to J_{sc}, V_{oc}, FF as can be observed from Figure 10 (b). At $N_{tr,H/A}$ =10^{14} cm^{-3} , the device η was 23.19 % and was decreased to 18.24% at $N_{tr,H/A}$ =10^{14} cm^{-3}, indicating high recombination at the

Preprints (www.preprints.org) | NOT PEER-REVIEWED | Posted: 7 July 2022 doi:10.20944/preprints202207.0104.v1

interface. Similarly, interface defect density at absorber layer/electron transport layer interface, $N_{tr,A/E}$. was also varied in the range of $10^{14} - 10^{17}$ (cm^{-3}). Unlike $N_{tr,H/A}$, $N_{tr,A/E}$ not significantly affected the device performance. The device η, V_{oc} , FF and J_{sc} retained their initial optimized values at $N_{tr,A/E}$ of $10^{14} - 10^{16}\ cm^{-3}$. However, η was slightly fallen to 23.83 % from 24.17% on a further increase in interface defects.

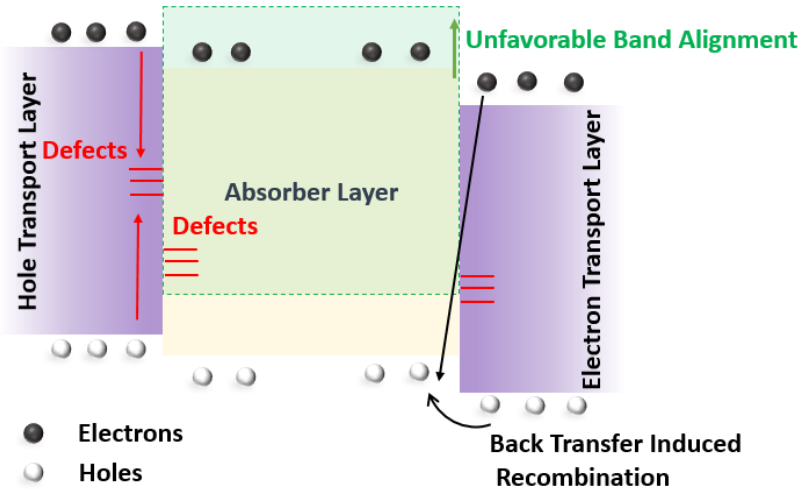

Figure 9. Illustration of Interface defects mechanism in a solar cell

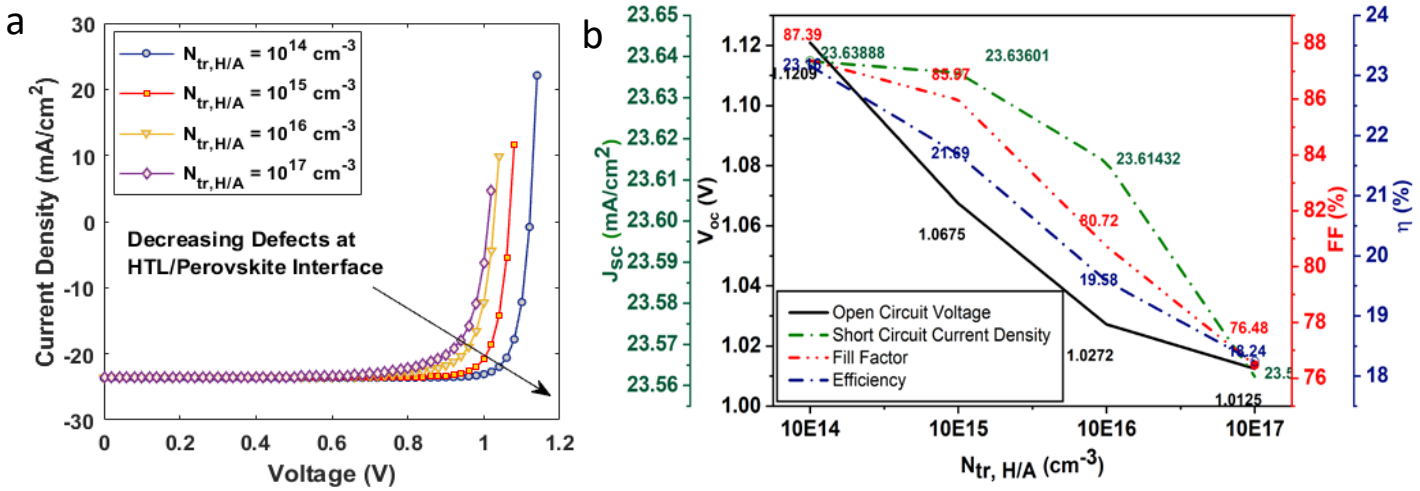

Figure 10. Current voltage characteristics of solar on inclusion of interface defects at hole transport layer/ absorber layer (b) Influence of interface defects on opencircuit voltage, short circuit current denisty , fill factor and efficiency of the solar cell

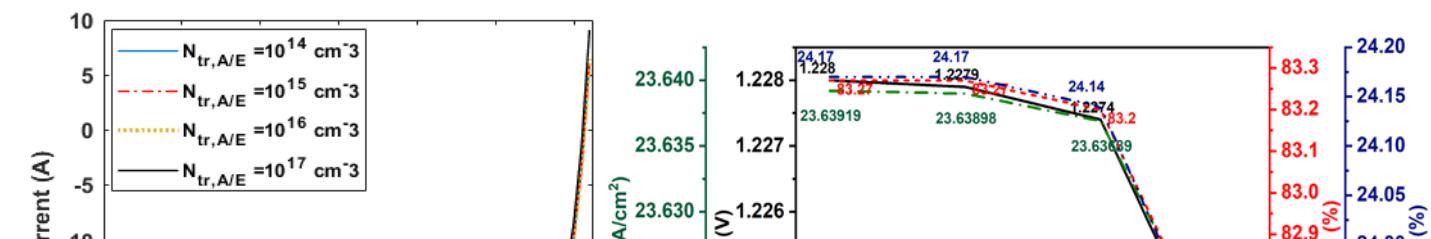

 doi:10.20944/preprints202207.0104.v1

Figure 11. Current voltage characteristics of solar on inclusion of interface defects at hole transport layer/ absorber layer (b) Influence of interface defects on opencircuit voltage, short circuit current denisty , fill factor and efficiency of the solar cell.

4. Conclusions

The combination of two absorber layers; carbon nitride, and perovskite absorber layer aided in the utilization of a broader range of solar spectrum for solar energy conversion. The device demonstrated high efficiency (24.17%), open-circuit voltage (1.2 V), and fill factor (83.2 %) with a uniform DOS energy bandgap. However, the focus is on computation investigation of dominant recombination mechanisms associated with the absorber layer to accurately investigate the device performance. The device η remained > 16% under higher radiative, auger coefficient, and trap-assisted recombination. Thereafter, we modeled the Gaussian distribution energy profile for shallow level defects and Urbach tail states for shallow level defects. This resulted in device efficiency falling to 22.14%. Further various double vacancy-based metastable defect states were induced in the absorber layer. It was observed that double donor metastable defects highly affect the performance of the solar cell. In the last, we also investigated the influence of interface defects. It was unveiled that for the proposed device architecture, increased defects in the HTL/absorber layer dominantly affected the device performance instead of absorber layer/ ETL interface defects.

Conflicts of Interest: Declare conflicts of interest or state "The authors declare no conflict of interest."

Nomenclature

Efficiency	η
Open Circuit Voltage	V_{oc}
Short Circuit Current Density	J_{sc}
Fill Factor	FF
Hole transport Layer	HTL
Electron Transport Layer	ETL
Double Absorber Layer	DAL
Wavelength	λ
Position dependent hole concentration	$p(x)$
Position dependent electron concentration	$n(x)$

 doi:10.20944/preprints202207.0104.v1

Shallow/Bulk carrier concentration	$N_{tr}{}^{\pm}$
electron hole pair generation	G
Minimum wavelength	λ_{min}
Maximum wavelength	λ_{max}
Transmission at front contact dependent on wavelength	$T_{front}(\lambda)$
Reflection at back contact dependent on wavelength	$R_{back}(\lambda)$
Internal reflection at front contact	$R_{int}(\lambda)$
Layer thickness	D
Energy bandgap	E_g
Optical absorption	α
Photon energy	E_p
Radiative recombination	R_{RAD}
Auger recombination	R_{AUG}
Schokley Read hall recombination	R_{SRH}
Radiative recombination coefficient	K
Auger electron recombination coefficient	$C_{n,aug}$
Auger hole recombination coefficient	$C_{p,aug}$
Electron concentration	n
Hole concentration	p
Intrinsic carrier concentration	n_i
Electron carrier life time	τ_n
Hole carrier life time	τ_p
Trap density of Double absorber layer	$N_{tr,DAL}$
Characteristic energy	E_c
Width of Gaussian energy distribution	w_g
Width of tail like distribution	w_t
Peak density of the distribution	N_{peak}
Energy trap level	E_t
Intrinsic energy level	E_i
Single donor defect states	$SD^{(0/+)}$
Double donor defect states	$DD^{(0/+/2/+}$
Single acceptor defect states	$SA^{(-/0)}$
Double acceptor defect states	$DA^{(2/-/0/-)}$
Interface defect density at hole transport layer/absorber layer interface	$N_{tr,H/A}$
Interface defect density at absorber layer /electron transport layer interface	$N_{tr,A/E}$

Appendix A. Layer parameters for numerical modeling of double absorber layer solar cell

Table A. Input layer parameters for numerical modeling of double absorber layer solar cell. The material parameters were adopted from the literature [16,40] as well as self-ascribed.

 doi:10.20944/preprints202207.0104.v1

References

Parameters	HTL	Perovskite	Carbon Nitride	ETL	FTO
Thickness (nm)	150	600	320	30	600
Energy Bandgap, E_g (eV)	3.04	1.55	1.8	3.2	3.5
Electron affinity, χ (eV)	2.2	3.9	4.2	4.1	4.0
Relative Permittivity, ε_r	3.0	6.5	4.5	9	9
Density of states at Conduction Band, N_c (cm^{-3})	2.5×10^{19}	2.5×10^{19}	2.5×10^{19}	2.5×10^{19}	2.5×10^{19}
Density of states Valance Band, N_v (cm^{-3})	2.5×10^{19}	2.5×10^{19}	2.5×10^{19}	2.5×10^{19}	2.5×10^{19}
Electron Mobility, μ_e (cm^2/Vs)	1.0×10^{-4}	2	12	5.0×10^{-2}	330
Hole Mobility, μ_h (cm^2/Vs)	1.0×10^{-4}	2	20	5.0×10^{-2}	50
Acceptor Concentration, N_a (cm^{-3})	1.0×10^{18}	2.0×10^{13}	0	0	0
Donor Concentration, N_d (cm^{-3})	0	3.0×10^{13}	1.0×10^{13}	1.0×10^{18}	2.0×10^{19}
Defect Density, N_t (cm^{-3})	1.0×10^{15}	1.0×10^{15}	1.0×10^{15}	1.0×10^{15}	1.0×10^{15}

1. Khalifa, S.A.; Mastrorocco, B. V; Au, D.D.; Ovaitt, S.; Barnes, T.M.; Carpenter, A.C.; Baxter, J.B. Dynamic material flow analysis of silicon photovoltaic modules to support a circular economy transition. *Prog. Photovoltaics Res. Appl.* **2022**, doi:10.1002/pip.3554.
2. Saeed, Faisal; Tauqeer, Haider Ali; Gelani, Hasan Erteza; Yousuf, Muhammad Hassan; Idrees, Asad Numerical modeling, simulation and evaluation of conventional and hybrid photovoltaic modules interconnection configurations under partial shading conditions. *EPJ Photovolt.* **2022**, *13*, 10, doi:10.1051/epjpv/2022004.
3. Mohsin, M.; Taghizadeh-Hesary, F.; Iqbal, N.; Saydaliev, H.B. The role of technological progress and renewable energy deployment in green economic growth. *Renew. Energy* **2022**, *190*, doi:10.1016/j.renene.2022.03.076.
4. Yan, D.; Cuevas, A.; Michel, J.I.; Zhang, C.; Wan, Y.; Zhang, X.; Bullock, J. Polysilicon passivated junctions: The next technology for silicon solar cells? *Joule* 2021, *5*.
5. Lameirinhas, R.A.M.; Torres, J.P.N.; de Melo Cunha, J.P. A Photovoltaic Technology Review: History, Fundamentals and Applications. *Energies* 2022, *15*.
6. Kim, S.; Hoang, V.Q.; Bark, C.W. Silicon-based technologies for flexible photovoltaic (Pv) devices: From basic mechanism to manufacturing technologies. *Nanomaterials* 2021, *11*.
7. Saeed, F.; Gelani, H.E. Unravelling the effect of defect density, grain boundary and gradient doping in an efficient lead-free formamidinium perovskite solar cell. *Opt. Mater. (Amst).* **2022**, *124*, doi:10.1016/j.optmat.2021.111952.
8. Saeed, F.; Waris, M.D.; Rehman, T.U.; Khan, M.A.; Khan, M.H.; Gelani, H.E. A Comparative Study of Grid-Tied PV Systems Employing CIGS and Crystalline Solar Modules. In Proceedings of the Proceedings of the 2021 Mohammad Ali Jinnah University International Conference on Computing, MAJICC 2021; 2021.
9. Qiao, Y.; Li, S.; Liu, W.; Ran, M.; Lu, H.; Yang, Y. Recent advances of Rare-Earth ion doped luminescent nanomaterials in perovskite solar cells. *Nanomaterials* 2018, *8*.
10. Mirbagheri, N.; Engberg, S.; Crovetto, A.; Simonsen, S.B.; Hansen, O.; Lam, Y.M.; Schou, J. Synthesis of ligand-free CZTS

nanoparticles via a facile hot injection route. *Nanotechnology* **2016**, *27*, doi:10.1088/0957-4484/27/18/185603.

11. Zhang, X.; Fu, E.; Zheng, M.; Wang, Y. Fabrication of Cu2ZnSnS4 thin films from ball-milled nanoparticle inks under various annealing temperatures. *Nanomaterials* **2019**, *9*, doi:10.3390/nano9111615.
12. Bottiglieri, L.; Nourdine, A.; Resende, J.; Deschanvres, J.L.; Jiménez, C. Optimized stoichiometry for CuCrO2 thin films as hole transparent layer in PBDD4T-2F: PC70BM organic solar cells. *Nanomaterials* **2021**, *11*, doi:10.3390/nano11082109.
13. Liu, J.; Aydin, E.; Yin, J.; Bastiani, M. De; Isikgor, F.H.; Rehman, A.U.; Yengel, E.; Ugur, E.; Harrison, G.T.; Wang, M.; et al. 28.2%-efficient, outdoor-stable perovskite/silicon tandem solar cell. *Joule* **2021**, *5*, doi:10.1016/j.joule.2021.11.003.
14. Ahmad, F.; Lakhtakia, A.; Monk, P.B. Double-absorber thin-film solar cell with 34% efficiency. *Appl. Phys. Lett.* **2020**, *117*, doi:10.1063/5.0017916.
15. Al-Ashouri, A.; Köhnen, E.; Li, B.; Magomedov, A.; Hempel, H.; Caprioglio, P.; Márquez, J.A.; Vilches, A.B.M.; Kasparavicius, E.; Smith, J.A.; et al. Monolithic perovskite/silicon tandem solar cell with >29% efficiency by enhanced hole extraction. *Science (80-.).* **2020**, *370*, doi:10.1126/science.abd4016.
16. Yasin, S.; Moustafa, M.; Zoubi, T. Al; Laouini, G.; Waar, Z.A. High efficiency performance of eco-friendly C2N/FASnI3 double-absorber solar cell probed by numerical analysis. *Opt. Mater. (Amst).* **2021**, *122*, doi:10.1016/j.optmat.2021.111743.
17. Yeon, D.H.; Mohanty, B.C.; Lee, S.M.; Cho, Y.S. Effect of band-aligned double absorber layers on photovoltaic characteristics of chemical bath deposited PbS/CdS thin film solar cells. *Sci. Rep.* **2015**, *5*, doi:10.1038/srep14353.
18. AlZoubi, T.; Moghrabi, A.; Moustafa, M.; Yasin, S. Efficiency boost of CZTS solar cells based on double-absorber architecture: Device modeling and analysis. *Sol. Energy* **2021**, *225*, doi:10.1016/j.solener.2021.07.012.
19. Mamta; Maurya, K.K.; Singh, V.N. Sb2Se3/CZTS dual absorber layer based solar cell with 36.32 % efficiency: A numerical simulation. *J. Sci. Adv. Mater. Devices* **2022**, *7*, doi:10.1016/j.jsamd.2022.100445.
20. Mahmood, J.; Lee, E.K.; Jung, M.; Shin, D.; Jeon, I.Y.; Jung, S.M.; Choi, H.J.; Seo, J.M.; Bae, S.Y.; Sohn, S.D.; et al. Nitrogenated holey two-dimensional structures. *Nat. Commun.* **2015**, *6*, doi:10.1038/ncomms7486.
21. Chen, Z.; Li, X.; Yang, J. The Contacts of the Monolayer Semiconductor C2N with 2D Metal Electrodes. *Adv. Theory Simulations* **2019**, *2*, doi:10.1002/adts.201800161.
22. Zhang, H.; Zhang, X.; Yang, G.; Zhou, X. Point Defect Effects on Photoelectronic Properties of the Potential Metal-Free C2N Photocatalysts: Insight from First-Principles Computations. *J. Phys. Chem. C* **2018**, *122*, doi:10.1021/acs.jpcc.7b12428.
23. Sun, J.; Zhang, R.; Li, X.; Yang, J. A many-body GW + BSE investigation of electronic and optical properties of C2N. *Appl. Phys. Lett.* **2016**, *109*, doi:10.1063/1.4963654.
24. Islam, M.S.; Sobayel, K.; Al-Kahtani, A.; Islam, M.A.; Muhammad, G.; Amin, N.; Shahiduzzaman, M.; Akhtaruzzaman, M. Defect study and modelling of SnX3-based perovskite solar cells with SCAPS-1D. *Nanomaterials* **2021**, *11*, doi:10.3390/nano11051218.
25. He, Y.; Xu, L.; Yang, C.; Guo, X.; Li, S. Design and numerical investigation of a lead-free inorganic layered double perovskite cs4cusb2cl12 nanocrystal solar cell by scaps-1d. *Nanomaterials* **2021**, *11*, doi:10.3390/nano11092321.
26. Yao, H.; Liu, L. Design and Optimize the Performance of Self-Powered Photodetector Based on PbS/TiS3 Heterostructure by SCAPS-1D. *Nanomaterials* **2022**, *12*, doi:10.3390/nano12030325.
27. Akhtaruzzaman, M.; Shahiduzzaman, M.; Amin, N.; Muhammad, G.; Islam, M.A.; Rafiq, K.S. Bin; Sopian, K. Impact of ar flow rates on micro-structural properties of ws2 thin film by rf magnetron sputtering. *Nanomaterials* **2021**, *11*, doi:10.3390/nano11071635.
28. Burgelman, M.; Decock, K.; Niemegeers, A.; Verschraegen, J.; Degrave, S. SCAPS Manual. *Univ. Gent* **2019**.

29. Luo, D.; Su, R.; Zhang, W.; Gong, Q.; Zhu, R. Minimizing non-radiative recombination losses in perovskite solar cells. *Nat. Rev. Mater.* 2020, *5*.

30. Riquelme, A.; Bennett, L.J.; Courtier, N.E.; Wolf, M.J.; Contreras-Bernal, L.; Walker, A.B.; Richardson, G.; Anta, J.A. Identification of recombination losses and charge collection efficiency in a perovskite solar cell by comparing impedance response to a drift-diffusion model. *Nanoscale* **2020**, *12*, doi:10.1039/d0nr03058a.

31. Shubham; Raghvendra; Pathak, C.; Pandey, S.K. Design, Performance, and Defect Density Analysis of Efficient Eco-Friendly Perovskite Solar Cell. *IEEE Trans. Electron Devices* **2020**, *67*, doi:10.1109/TED.2020.2996570.

32. Mehdizadeh-Rad, H.; Singh, J. Influence of Urbach Energy, Temperature, and Longitudinal Position in the Active Layer on Carrier Diffusion Length in Perovskite Solar Cells. *ChemPhysChem* **2019**, *20*, doi:10.1002/cphc.201801038.

33. Belaroussi, T.; Rached, D.; Rahal, W.L.; Hamdache, F. Sensitivity of a HIT c-Si Solar Cell to Structural Distortions of the Hydrogenated Amorphous Silicon Constituting the Front Face of the Device. *J. Nano- Electron. Phys.* **2020**, *12*, doi:10.21272/jnep.12(5).05023.

34. Samiee, M.; Konduri, S.; Ganapathy, B.; Kottokkaran, R.; Abbas, H.A.; Kitahara, A.; Joshi, P.; Zhang, L.; Noack, M.; Dalal, V. Defect density and dielectric constant in perovskite solar cells. *Appl. Phys. Lett.* **2014**, *105*, doi:10.1063/1.4897329.

35. Zhou, Y.; Poli, I.; Meggiolaro, D.; Angelis, F. De; Petrozza, A. Defect activity in metal halide perovskites with wide and narrow bandgap. *Nat. Rev. Mater.* 2021, *6*.

36. Burgelman, M.; Decock, K.; Khelifi, S.; Abass, A. Advanced electrical simulation of thin film solar cells. In Proceedings of the Thin Solid Films; 2013; Vol. 535.

37. Ball, J.M.; Petrozza, A. Defects in perovskite-halides and their effects in solar cells. *Nat. Energy* **2016**, *1*, doi:10.1038/nenergy.2016.149.

38. Shukla, S.; Sood, M.; Adeleye, D.; Peedle, S.; Kusch, G.; Dahliah, D.; Melchiorre, M.; Rignanese, G.M.; Hautier, G.; Oliver, R.; et al. Over 15% efficient wide-band-gap Cu(In,Ga)S2 solar cell: Suppressing bulk and interface recombination through composition engineering. *Joule* **2021**, *11*, doi:10.3390/nano11010219.

39. Green, M.A.; Ho-Baillie, A.; Snaith, H.J. The emergence of perovskite solar cells. *Nat. Photonics* 2014, *8*.

40. Raoui, Y.; Ez-Zahraouy, H.; Tahiri, N.; Bounagui, O. El; Ahmad, S.; Kazim, S. Performance analysis of MAPbI3 based perovskite solar cells employing diverse charge selective contacts: Simulation study. *Sol. Energy* **2019**, *193*, doi:10.1016/j.solener.2019.10.009.